Effects of rare-earth size on the electronic structure of $La_{1-x}Lu_xVO_3$

2015 J. Phys.: Condens. Matter 27 105503

(http://iopscience.iop.org/0953-8984/27/10/105503)

IOP Publishing Journal of Physics: Condensed Matter

J. Phys.: Condens. Matter **27** (2015) 105503 (13pp) doi:10.1088/0953-8984/27/10/105503

Effects of rare-earth size on the electronic structure of $La_{1-x}Lu_xVO_3$

B Chen[1], J Laverock[1], D Newby Jr[1], J F McNulty[1], K E Smith[1,4], P-A Glans[2], J-H Guo[2], R-M Qiao[2], W-L Yang[2], M R Lees[3], L D Tung[3,5], R P Singh[3,6] and G Balakrishnan[3]

[1] Department of Physics, Boston University, 590 Commonwealth Avenue, Boston, MA 02215, USA
[2] Advanced Light Source, Lawrence Berkeley National Laboratory, Berkeley, CA 94720, USA
[3] Department of Physics, University of Warwick, Coventry, CV4 7AL, UK
[4] School of Chemical Sciences and The MacDiarmid Institute for Advanced Materials and Nanotechnology, The University of Auckland, Auckland 1142, New Zealand

E-mail: bchen727@bu.edu

Received 7 November 2014, revised 18 January 2015
Accepted for publication 2 February 2015
Published 24 February 2015

Abstract

The electronic structure of $La_{1-x}Lu_xVO_3$ ($x = 0$, 0.2, 0.6 and 1) single crystals has been investigated using soft x-ray absorption spectroscopy, soft x-ray emission spectroscopy, and resonant soft x-ray inelastic scattering to study the effects of rare-earth size. The x-ray absorption and emission spectra at the O K-edge present a progressive evolution with R-site cation, in agreement with local spin density approximation calculations. This evolution with R, together with the temperature dependence of the O K-edge spectra, is attributed to changes in the crystal structure of $La_{1-x}Lu_xVO_3$. The crystal-field dd* excitations probed by resonant inelastic x-ray scattering at the V L_3-edge exhibit an increase in energy and enhanced intensity with the decrease of R-site ionic radius, which is mainly attributed to the increased tilting magnitude of the VO_6 octahedra. Upon cooling to ~95 K, the dd* excitations are prominently enhanced in relative intensity, in agreement with the formation of the Jahn–Teller distortion in the orbital ordering phase. Additionally, the dd* transitions of the mixed compounds are noticeably suppressed with respect to those of the pure compounds, possibly owing to the formation of C-type orbital ordering induced by large R-site size variances.

Keywords: x-ray absorption spectra, x-ray emission spectra and fluorescence, resonant inelastic x-ray scattering, local spin density approximation, electron density of states, strongly correlated electron systems

(Some figures may appear in colour only in the online journal)

1. Introduction

The transition-metal oxides RMO_3 (R = rare earth or yttrium, M = transition metal) with the perovskite-type structure form a very important group of strongly correlated electron systems, and exhibit a complex interplay between spin, charge, orbital and lattice degrees of freedom. Owing to the crystal field of the MO_6 octahedron, the M 3d orbitals are split into near-degenerate t_{2g} (three-fold) and e_g (two-fold) levels. In contrast to the strong Jahn–Teller (JT) coupling in the e_g manganites, $RMnO_3$, the orbital–lattice interaction in t_{2g}-active vanadates, RVO_3, is much weaker and is comparable to the spin–spin interaction [1, 2]. Consequently, unlike $RMnO_3$, spin ordering (SO) and orbital ordering (OO) compete at similar temperatures and the interplay between the different degrees of freedom is more complex in RVO_3 [1, 2].

In RVO_3, the V^{3+} t_{2g} orbitals are doubly occupied, with one electron in the d_{xy} level and the other in either the d_{yz} or d_{zx} levels. Together with the spin degree of freedom, this two-fold occupation of the three-fold degenerate t_{2g} orbitals offers

[5] Present address: Department of Physics and Astronomy, University College London, Gower Street, WC1E 6BT, London, UK.
[6] Present address: Department of Physics, IISER Bhopal, Madhya Pradesh 462023, India.

two possible kinds of orbital-ordered and spin-ordered states, referred to as G-type and C-type order, and the particular ground state that is favoured depends on the R-site cation. Each type of OO is associated with a particular V 3d–O 2p bonding pattern due to the JT distortion, which gives rise to short and long V–O distances [3, 4]. In the G-type OO, the $d_{xy}d_{yz}$ and $d_{xy}d_{zx}$ orbitals are alternately occupied on adjacent vanadium sites along all three crystal axes, with the V–O distances arranged 'out of phase' between successive *ab* planes [3, 4]. For C-type OO, the electron configurations are alternate $d^1_{xy}d^1_{yz}/d^1_{xy}d^1_{zx}$ in the *ab* plane and identical along the c-axis, with an 'in phase' arrangement of the V–O distances in successive *ab* planes [3, 4].

The phase diagram of RVO$_3$ has been extensively studied, and reveals a fascinating complexity in different types of order with temperature, R-site ionic size, and R-site substitution [1, 2, 5, 6]. Below $T_{OO1} \sim 200$ K, RVO$_3$ exhibits a transition to an orbital-ordered state with G-type occupation, concomitantly with a structural phase transition. For CeVO$_3$ and LaVO$_3$ (both of which have a larger R cation), this structural transition appears just below the antiferromagnetic (AFM) transition, $T_{SO1} \sim 100$ K. For the smaller rare-earth ions (R = Lu − Dy), an additional transition occurs at $T_{SO2} = T_{OO2} \sim 80$ K, in which the OO switches to the C-type configuration. For example, resonant x-ray scattering has confirmed the existence of the two types of orbital-ordered states in the low-temperature phase of YVO$_3$ [3, 7]. When partially substituted with other rare-earth members in the parent RVO$_3$ compound, for instance $Y_{1-x}La_xVO_3$ [6], $Y_{1-x}(La_{0.2337}Lu_{0.7663})_xVO_3$ [6]. and Eu_{1-x} $(La_{0.254}Y_{0.746})_x$ VO_3 [5], the size mismatch of the different R-site cations induces a structural disorder. For dilute doping, an increase in the substitution content x, leads to a linear increase in the size variance (SV), defined as $\langle r_i^2\rangle - \langle r_i\rangle^2$ (r_i is the R-site ionic radius), which has the effect of stabilizing the C-type OO at the expense of the G-type OO. Coincidently, T_{OO1} and T_{SO1} are steadily decreased and the transitions accompanied by G-OO vanish above a critical x content, while $T_{SO2} = T_{OO2}$ of the transition with the formation of C-OO is progressively enhanced [5, 6]. Lastly, this spin–orbital phase diagram of RVO$_3$ was additionally reported to evolve with hydrostatic pressure [8] and hole doping [9].

At room temperature, the perovskite-type RVO$_3$ resides in an orthorhombic crystal structure (space group *Pbnm*, No. 62) with unit-cell parameters of $a \approx b \approx \sqrt{2}a_0, c \approx 2a_0$, where the lattice constant of an ideal cubic perovskite, $a_0 \approx 3.8$ Å [10]. The VO$_6$ octahedra are highly distorted, rotated and tilted with respect to each other in order to relieve the structural stress. As the R-site cation varies, the crystal structure of RVO$_3$ evolves: in particular, with the decrease of R-site size from La to Lu, the unit-cell volume progressively shrinks [10]. Meanwhile, the distortion of the VO$_6$ octahedra, characterized by the tilting angle, $\varphi = (180^\circ - \langle V - O - V\rangle)/2$, is gradually enhanced [10]. On the other hand, the ionic radius of the rare-earth (lanthanide) series increases with the R-site cation varied from La to Lu. While the structural aspects of R-site substitution have been well characterized, their effects on the electronic structure of RVO$_3$ remain unclear. In the pure compounds, optical spectroscopy has been used to measure the inter-site dd* excitations of the V t_{2g} electrons across two adjacent vanadium sites (dimer-type excitations) [11, 12]. For example, the optical strength of the dimer excitations of YVO$_3$ was found to display strong dependence with temperature upon cooling down across phase transitions, in agreement with the formation of OO [11]. Transition metal L-edge resonant inelastic soft x-ray scattering (RIXS), on the other hand, probes the on-site dd* excitations, providing direct information on the local electronic structure and crystal field of RVO$_3$ [13–15]. In addition to the local crystal-field excitations, a delocalized orbital excitation, in the form of a bi-orbiton involving the exchange of orbitals between adjacent sites, has also been reported at ∼0.4 eV in YVO$_3$, HoVO$_3$ [12, 13] and NdVO$_3$ [14] via optical spectroscopy and RIXS.

We report here a comprehensive study of the electronic structure of the $La_{1-x}Lu_xVO_3$ system, which covers the largest and smallest R ionic sizes, respectively. Soft x-ray spectroscopy measurements are employed to access the bulk occupied and unoccupied densities of states, as well as their elementary excitations, and are combined with *ab initio* calculations of the electronic structure.

2. Methods

2.1. Experiments

Single crystals of $La_{1-x}Lu_xVO_3$ (x = 0, 0.2, 0.6 and 1) were grown by the floating zone technique using a high-temperature xenon lamp optical furnace at the University of Warwick [16]. $La_{1-x}Lu_xVO_3$ (x = 0, 0.2, 0.6 and 1) solid solutions were selected to investigate both the largest and smallest rare-earth ionic radii, as well as the medium rare-earth ionic size. In addition, the R-site substitution of the doped $La_{1-x}Lu_xVO_3$ compounds introduces a substantial R-site SV. The quality of the crystals was examined using Laue back-reflection diffraction. The magnetization and heat-capacity measurements of $La_{0.8}Lu_{0.2}VO_3$ and $La_{0.4}Lu_{0.6}VO_3$ crystals were carried out using a Quantum Design (QD) Magnetic Property Measurement System (MPMS) superconducting quantum interference device (SQUID) magnetometer and a QD Physical Property Measurement System (PPMS), respectively. During the magnetization measurements, the sequences of zero-field-cooled warming (ZFCW), field-cooled cooling (FCC) and field-cooled warming (FCW) were performed with an applied magnetic field of 1 kOe.

The soft x-ray measurements were performed at the AXIS and SXF end-stations of Beamlines 7.0.1 and 8.0.1 of the Advanced Light Source, Lawrence Berkeley National Laboratory. $La_{1-x}Lu_xVO_3$ single crystals were cleaved in air to expose fresh surfaces, and then immediately loaded into the experimental chamber with an ultra-high vacuum pressure of $< 1 \times 10^{-9}$ Torr. The x-ray absorption spectroscopy (XAS) spectra were measured in both total electron yield (TEY) and total fluorescent yield (TFY) detection modes with an incident photon energy resolution of ∼0.20 eV at the O K-edge. The x-ray emission spectroscopy (XES) and RIXS spectra were recorded with emission spectrometer resolutions at the O K-edge of 0.37 eV and 0.28 eV at Beamlines 7.0.1 and 8.0.1,

respectively. The XAS photon energy scale was calibrated using the O K-edge and Ti L-edge absorption peaks of rutile TiO_2 [17]. The XES spectrometer energy scale was calibrated using metal Zn L-shell emission lines in second order [15].

2.2. Electronic structure calculations

The self-consistent electronic structures of $LaVO_3$ and $LuVO_3$ were calculated within the local spin density approximation (LSDA), including the static Coulomb repulsion parameter U (LSDA + U), using the all-electron full-potential linearized augmented plane wave (FLAPW) method implemented by the ELK code [18]. The well-known problems associated with describing localized rare-earth 4f electrons within the LSDA were circumvented by applying $U = 6.8$ eV to the R 4f shell [19], corresponding to fully unoccupied and fully occupied 4f states for $LaVO_3$ and $LuVO_3$, respectively. The localized V 3d states were treated using $U = 3.4$ eV and $J = 0.85$ eV [11], with a ferromagnetic spin structure. Although the system is paramagnetic at room temperature, a magnetic solution is necessary to obtain the correct local 3d electronic structure [20]. Secondly, the local partial densities of states are relatively insensitive to the long-range magnetic structure, showing only weak differences between ferromagnetic and AFM structures. Convergence was achieved on 64 k-points in the orthorhombic (1/8th) irreducible Brillouin zone using the room temperature lattice parameters given by [10], and with a cutoff for plane waves in the interstitial region of $k_{max} = 7.5/R_{min}$, where R_{min} is the O muffin-tin radius. Muffin-tin radii of 2.2 atomic units (au), 2.0 au and 1.6 au were used for R, V and O, respectively. Equivalent calculations were also performed replacing La and Lu with Y in the same $LaVO_3$ and $LuVO_3$ crystal structures (and denoted $Y_{La}VO_3$ and $Y_{Lu}VO_3$), to check whether the origin of any differences were due to the crystal structure (bond lengths and angles etc) or to the specific choice of rare earth (e.g. d electron energies).

The partial densities of states of O, V and R from the LSDA + U calculations of $LaVO_3$ and $LuVO_3$ are shown in figure 1. The R 4f states are located at ~ -4.6 eV in the occupied O 2p manifold for $LuVO_3$ and at $\sim$9.5 eV in the unoccupied manifold for $LaVO_3$ in figure 1. Below the Fermi level (E_F), the O 2p manifold extends to -2.7 eV, above which the doubly occupied V $t_{2g\uparrow}$ states are located. Owing to the greater distortions to the VO_6 octahedra in $LuVO_3$, the bandwidth of the LSDA + U V t_{2g} states are narrower in this compound by $\sim$15%. Above E_F, the unoccupied spin-polarized V t_{2g} states appear at lower energy, after which the V e_g bands mix with La and Lu 5d states. The differences between the electronic structures of $LaVO_3$ and $LuVO_3$ are mostly driven by the lower energy of the La 5d orbitals compared with Lu 5d, which leads to enhanced R–O covalency, and the stronger distortion of the VO_6 octahedra in $LuVO_3$, which leads to weaker overlap between orbitals. Similar variation of V 3d states with R, although weaker, is also found in corresponding electronic structures of YVO_3 calculated within both $LaVO_3$ and $LuVO_3$ crystal structures, suggesting its origin partly arises from the evolution of the crystal structure of RVO_3.

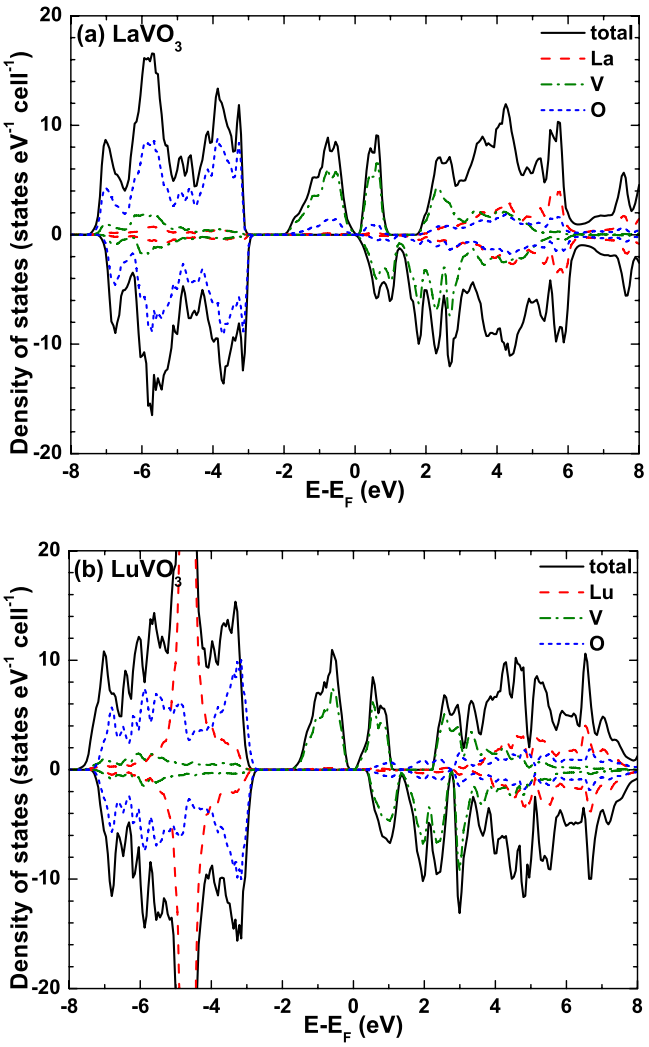

Figure 1. Partial densities of states of (*a*) $LaVO_3$ and (*b*) $LuVO_3$ from FLAPW LSDA + U calculations.

3. Results and discussion

3.1. Magnetization and heat capacity

Figure 2 presents the temperature dependence of the magnetic susceptibility and the specific heat of $La_{0.8}Lu_{0.2}VO_3$ and $La_{0.4}Lu_{0.6}VO_3$ crystals. For the zero-field-cooled (ZFC) measurement, the samples were cooled down to 5 K in zero magnetic field, a field of 1 kOe was applied, and the susceptibility data were then recorded on warming. The field-cooled (FC) data were then collected on a subsequent cooling and warming of the sample in the same applied field. The heat capacity data were collected warming from base temperature. The magnetic contribution to the specific heat is obtained by subtracting the phonon contribution to the specific heat, which was estimated by fitting a Debye–Einstein function to the data at temperatures away from any magnetic and structural transitions. Magnetic susceptibility and specific heat measurements of the pure $LaVO_3$ and $LuVO_3$ compounds have been reported elsewhere [2, 16, 21].

Only one phase transition is observed in $La_{0.4}Lu_{0.6}VO_3$ (SV $= 8.0 \times 10^{-3}$ Å^2) between room temperature and 5 K. As

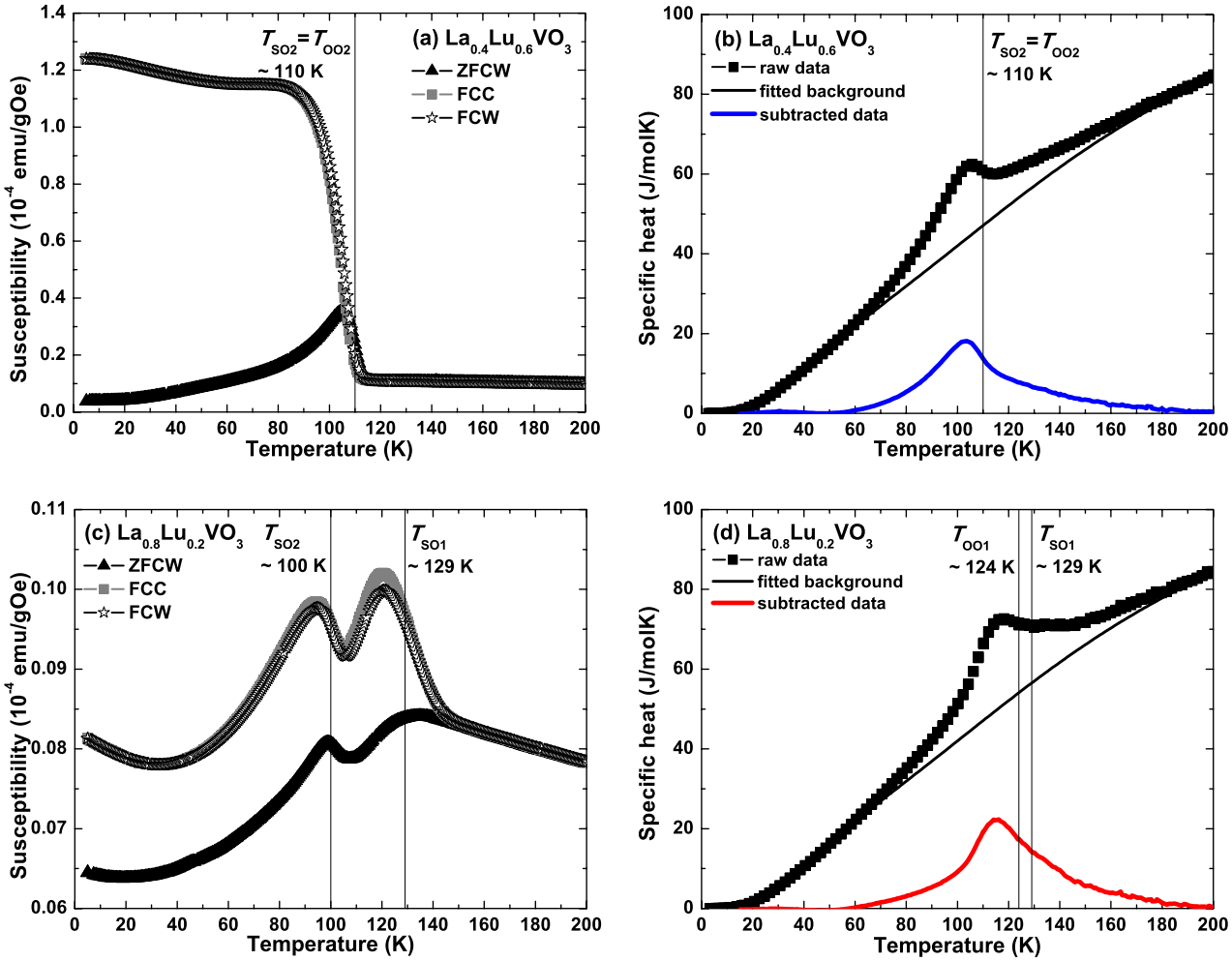

Figure 2. Temperature dependence of the susceptibility and the specific heat of $La_{0.4}Lu_{0.6}VO_3$ ((*a*) and (*b*), respectively) and $La_{0.8}Lu_{0.2}VO_3$ ((*c*) and (*d*), respectively). The susceptibility data were recorded during ZFCW (black filled triangles), FCC (grey filled squares) and FCW (black empty stars). The phonon contribution (black solid line) to the specific heat was estimated by fitting a Debye–Einstein function to the data (black filled squares) at temperatures away from any magnetic and structural transitions. The data after subtraction represents the magnetic contribution to the specific heat of $La_{0.4}Lu_{0.6}VO_3$ (blue solid line) and $La_{0.8}Lu_{0.2}VO_3$ (red solid line). The SO and OO temperatures are indicated by vertical lines.

shown in figure 2(*a*), the susceptibility of $La_{0.4}Lu_{0.6}VO_3$ displays a sharp magnetic transition at T_{SO2}=T_{OO2}~110 K, suggesting the onset of SO. At the same temperature, the specific heat of $La_{0.4}Lu_{0.6}VO_3$ exhibits an anomaly in figure 2(*b*), indicating a structural transition accompanied by OO. Qualitatively, our data resembles $Y_{1-x}La_xVO_3$ (SV $\gtrsim 3 \times 10^{-3}$ Å^2) [6], Y_{1-x} $(La_{0.2337}Lu_{0.7663})_x$ VO_3 (SV $\gtrsim 3 \times 10^{-3}$ Å^2) [6], and Eu_{1-x} $(La_{0.254}Y_{0.746})_x$ VO_3 (SV $\gtrsim 5 \times 10^{-3}$ Å^2) [5], and we therefore attribute the transition to the formation of *C*-type OO and *G*-type SO. For those doped compounds, a series of samples with successive doping contents were studied to investigate the detailed evolution of the OO and SO states with the SV, which shed light on similar *R*-site mixed systems. For $x = 0.2$, the SV is much smaller at 5.4×10^{-3} Å^2, and several transitions are observed in $La_{0.8}Lu_{0.2}VO_3$. As shown in figure 2(*c*), the susceptibility of $La_{0.8}Lu_{0.2}VO_3$ displays two weak, but visible, magnetic transitions at $T_{SO1} \sim 129$ K and $T_{SO2} \sim 100$ K, respectively. The high-temperature magnetic transition corresponds to a shoulder feature of the specific heat in figure 2(*d*), which is followed by a peak at $T_{OO1} \sim 124$ K resulting from a structural transition. The presence of these two transition temperatures (T_{SO1} and T_{OO1}) arises from the residue of *C*-type SO and *G*-type OO in $La_{0.8}Lu_{0.2}VO_3$ and the occurrence of OO just below SO resembles that of $LaVO_3$ [16, 21]. The lower temperature magnetic transition at $T_{SO2} \sim 100$ K is most likely associated with the development of *G*-type SO in $La_{0.8}Lu_{0.2}VO_3$. However, around this temperature, no corresponding structural transition is visible (or, if it is present, it is not visible in the data) in the broad feature of the specific heat in figure 2(*d*). The absence (or the very weak appearance) of this structural transition indicates that the *C*-type OO either has not formed or is just developing in $La_{0.8}Lu_{0.2}VO_3$.

3.2. X-ray absorption spectroscopy

The XAS process involves the excitation of a core electron into the conduction band (CB) by an incident photon, and is governed by dipole selection rules. At the O *K*-edge of transition-metal oxides, XAS approximately reflects the unoccupied O 2p partial density of states (PDOS) of the CB

in the presence of a core hole [22]. The overall effect of the core hole on the shape of the measured spectrum is generally weak at the O K-edge, principally owing to the localization of the core hole at the O site, away from the transition-metal ion, whose states dominate the CB [23]. However, it does lead to an appreciable shift upwards in energy by ≈1.0 eV in typical metal oxides [24]. The situation is different at the transition-metal L-edge, where the XAS process is dominated by the strong interactions between the 2p core hole and the 3d valence wave functions, i.e. multiplet effects [25, 26]. Experimentally, the XAS spectrum can be recorded in either TEY or TFY modes, and both methods have been employed here. In TEY, the sample drain current is collected, leading to a greater surface sensitivity with a sampling depth of ∼10 nm, whereas in TFY mode, the emitted photon due to the decay of the excited electron in the CB to fill the core hole is detected. Consequently, TFY probes a sample depth of ∼100 nm, i.e. it is more bulk sensitive, although it does suffer from self-absorption effects [27].

Figure 3(a) shows normalized (to the maximum intensity) XAS-TFY spectra at the V $L_{3,2}$-edge of several $La_{1-x}Lu_xVO_3$ compounds measured at room temperature. The corresponding TEY spectra are qualitatively very similar. The V $L_{3,2}$-edge XAS spectra present a typical structure of two main absorption peaks, located at ∼517 eV (L_3 edge) and ∼524 eV (L_2 edge), owing to transitions from the spin–orbit split $2p_{3/2}$ and $2p_{1/2}$ core levels to unoccupied V 3d orbitals. These spectra are similar to previous XAS measurements of other RVO_3 compounds, and agree well with atomic multiplet calculations of the d^2 V^{3+} ion [14, 28]. The L_3-edge spectra are composed of two pre-edge features B (∼513.6 eV) and C (∼515.2 eV) with t_{2g} character and a main absorption peak E (∼517.4 eV) of e_g character [14]. Overall, the spectra are very similar for different R, reflecting the similarity of the V local environment and V 3d electronic structure through the series. However, there are some weak, discernible changes with R: the shoulder marked by the triangle at 518.8 eV in figure 3(a) is more prominent for $LaVO_3$, reflecting the slight transfer in weight from peak E to higher energies in this compound. Local multiplet effects dominate the structure of the V L_3-edge absorption spectrum; however, it is difficult to account for the subtle evolution in this shoulder from crystal field arguments without introducing discrepancies elsewhere. Instead, we interpret its behaviour from the perspective of the band structure, which is known to be important in the V L_3-edge spectra of metallic quasi-perovskites such as $Sr_xCa_{1-x}VO_3$ [14, 28]. In figure 3(b), the theoretical (spin-averaged) unoccupied V 3d PDOS of $LaVO_3$ and $LuVO_3$ are shown after accounting for instrument and lifetime broadening. For $LaVO_3$, a strong shoulder develops on the high-energy side of the e_g peak due to mixing of the V e_g orbitals with La 5d states. In $LuVO_3$, the Lu 5d states are located almost 1 eV higher in energy and experience weaker mixing with the V e_g orbitals, leading to a weaker shoulder in agreement with the experiment. Although local multiplet effects clearly dominate the V L-edge XAS spectra, this observation indicates the (albeit weak) influence of the delocalized PDOS in a wide band-gap insulator.

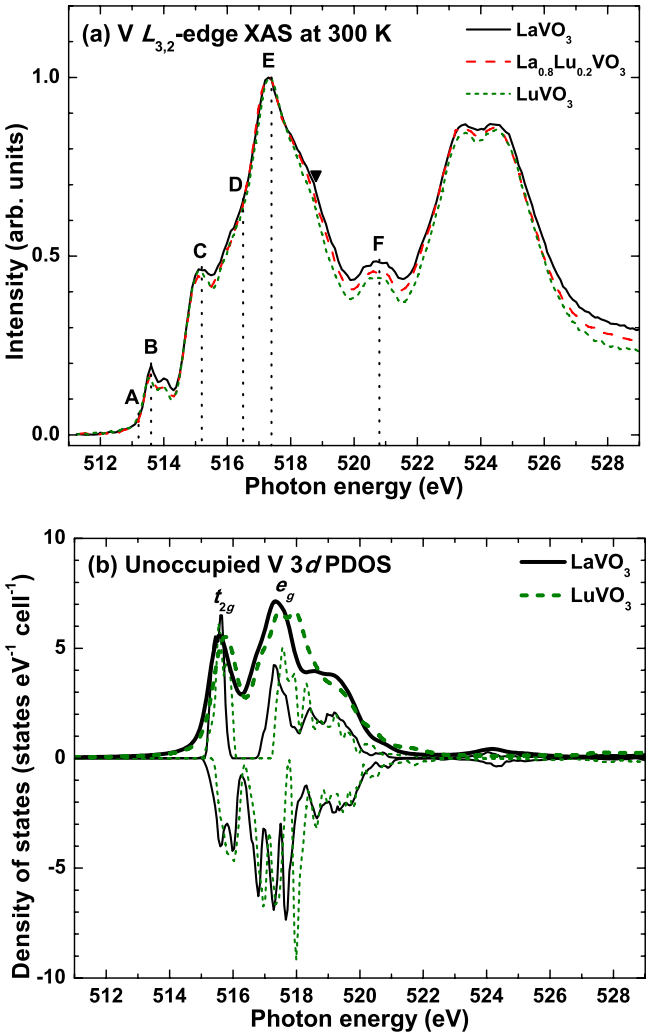

Figure 3. (a) Normalized V $L_{3,2}$-edge XAS-TFY spectra of $La_{1-x}Lu_xVO_3$($x = 0$, 0.2 and 1) compounds measured at room temperature. The photon energies of the L_3-edge XAS absorption threshold A and spectral features B–F are indicated by vertical dotted lines, and the triangle indicates the e_g shoulder at 518.8 eV. (b) Unoccupied V 3d PDOS of $LaVO_3$ (black solid line) and $LuVO_3$ (olive short dash line) from the FLAPW calculations, offset by the V L_3-edge threshold energy of 515.0 eV. Thick lines show the spin-averaged, broadened PDOS, whereas thin lines correspond to the raw band calculation.

Figure 4(a) presents normalized XAS-TFY spectra at the O K-edge of $La_{1-x}Lu_xVO_3$ compounds at room temperature, with the energies of some of the prominent spectral features indicated by (a–h) for $LaVO_3$. For comparison, the spin-averaged O 2p PDOS of $LaVO_3$ and $LuVO_3$ from the LSDA + U calculations are shown in figure 4(b), after convolution with a Lorentzian of 0.22 eV half-width at half-maximum (HWHM, to approximate the lifetime broadening of the O 1s core hole) and a Gaussian of 0.20 eV full-width at half-maximum (FWHM, to account for the instrument resolution function) [29].

Good agreement is obtained between the experimental XAS spectra at the O K-edge and the theoretical LSDA + U O 2p PDOS. At low energies (⩽8 eV), the CB is dominated by V 3d and R 5d states, which are well reproduced by the LSDA+U. Feature a (∼530.4 eV) can be associated with excitations into

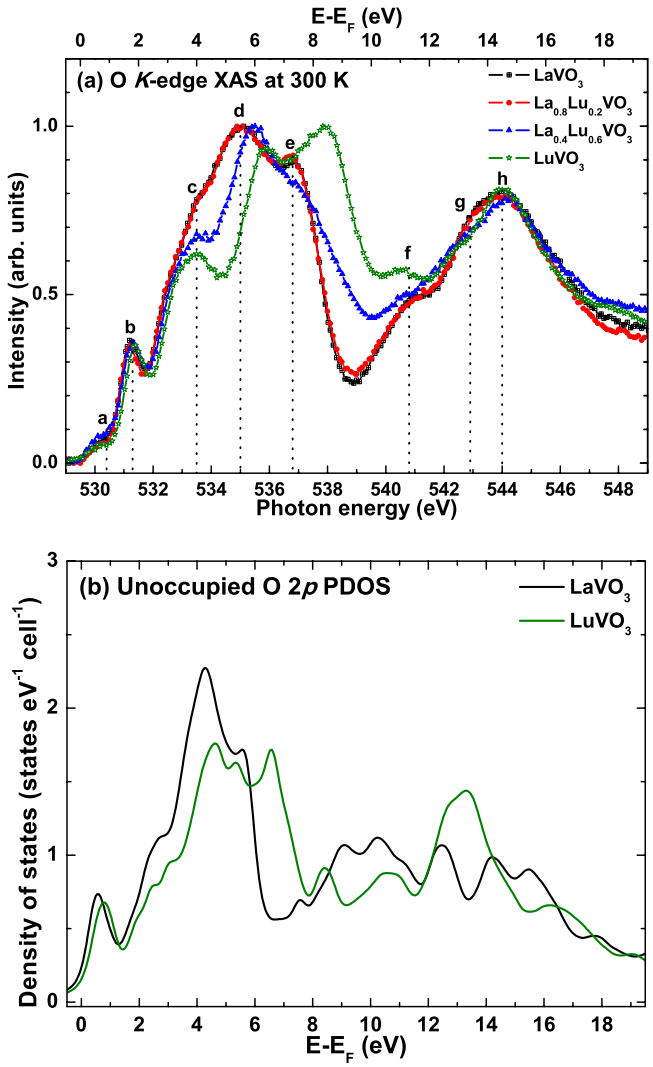

Figure 4. (*a*) Normalized O *K*-edge XAS-TFY spectra of $La_{1-x}Lu_xVO_3$ ($x = 0$, 0.2, 0.6 and 1) compounds recorded at room temperature. Both a calibrated photon energy scale (bottom axis) and an approximate binding energy scale (top axis) are displayed in (*a*). The photon energies of the O *K*-edge XAS spectral features *a*–*h* are marked by vertical dotted lines for $LaVO_3$. (*b*) A comparison of the theoretical O 2p PDOS of the CB between $LaVO_3$ (black solid line) and $LuVO_3$ (olive solid line).

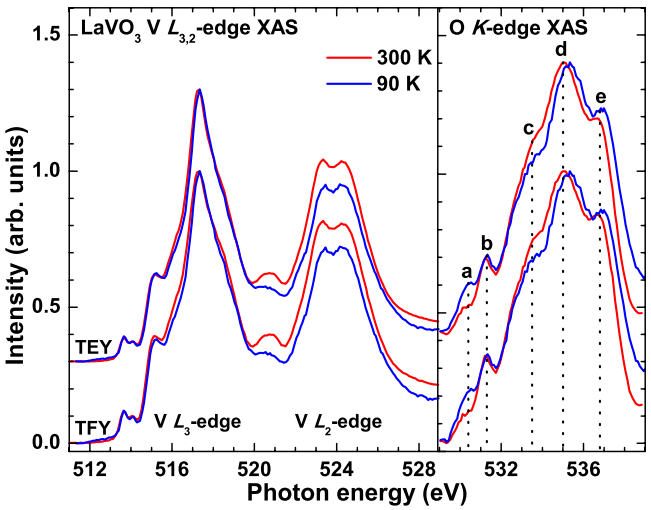

Figure 5. Normalized V $L_{3,2}$-edge and O *K*-edge XAS spectra of $LaVO_3$ measured at both ~300 K (red lines) and ~90 K (blue lines). The XAS spectra were recorded in both TEY (with offset) and TFY (without offset) modes. The labels (*a*–*e*) represent the same features indicated in figure 4(*a*).

unoccupied $t_{2g\uparrow}$ states, and *b* (~531.3 eV) with V $t_{2g\uparrow}$ states, whereas *c* (533.5 eV) originates from O 2p–V e_g hybridized states. In the LSDA + *U* calculation, the $t_{2g\uparrow}$ and $t_{2g\downarrow}$ states are very close in energy, but are found to be more strongly separated experimentally. Consistent with our measurements at the V *L*-edge, and with the LSDA + *U*, these features do not evolve significantly with *x*, reinforcing the similarity in V local environment across the series. Note that the apparent slight shift upwards in the energy of feature *c* for $LuVO_3$ in the LSDA + *U* calculation (figure 4(*b*)) is mostly due to additional contributions from *R* 5d states at higher energies, and that the unoccupied V PDOS does not exhibit such a strong shift (see figure 1). This additional contribution from La 5d states (which appear at a lower energy than the Lu 5d states) also accounts for the stronger relative intensity of feature *c* in $LaVO_3$. Features *d* (~535.0 eV for $LaVO_3$) and *e* (~536.8 eV for $LaVO_3$), located at the absorption peak, mainly arise from O 2p–*R* 5d hybridization, in agreement with previous studies of $LaVO_3$ and YVO_3 [28, 30, 31], and the energies of these features, and their evolution with *R*, are predicted well by the LSDA + *U* calculation. The apparent similarity of the $x = 0.2$ spectrum to that of pure $LaVO_3$ is due to the light Lu doping; the O *K*-edge XAS of $La_{0.8}Lu_{0.2}VO_3$ is dominated by the contribution from La and V sites. Finally, at higher energies features *f*–*h* are mostly due to V 4sp hybridization, consistent with YVO_3 [28] as well as other vanadium oxides [20, 32, 33]. We note that these states are not captured well by the theoretical PDOS, although at such high energies above E_F the accuracy of any linearized DFT method must be questioned.

We now turn to the temperature dependence of the XAS. Figure 5 shows V $L_{3,2}$-edge and O *K*-edge XAS spectra of $LaVO_3$ collected at both room temperature and low temperature (~90 K), and in both TEY and TFY modes in order to probe the surface and bulk absorption signals from the sample, respectively. Our V $L_{3,2}$-edge XAS spectra are absent of surface contamination signals owing to V^{4+} and V^{5+} oxidization states [34] (usually located at ~2 eV above the V^{3+} main absorption peak), which indicates a clean sample surface during the measurements.

Upon cooling down to 90 K (AFM *C*-SO phase), the spectral width of the V L_3-edge appears slightly narrowed and the branching ratio, $I_{L_3}/\left(I_{L_3}+I_{L_2}\right)$, becomes notably stronger. Whilst the weak narrowing of the L_3 edge has been attributed to the small change in the local V crystal-field at low temperature, the evolution in the branching ratio is in contrast to similar measurements of $NdVO_3$ at ~100 K [14], and is not expected from the weak evolution in crystal-field splitting [35]. Such temperature-dependent XAS measurements are very sensitive to the quality of the sample surface and vacuum, since at cryogenic temperatures the sample can act as a cold trap in a poor vacuum. Here, every effort has been made to minimize extrinsic effects, and the absence of surface

contaminant species in both V L- and O K-edges at both temperatures, and the similarity between surface- (TEY) and bulk-sensitive (TFY) probes, support an intrinsic origin for this evolution. Similar enhancements to the branching ratio have previously been observed at transition-metal $L-$edges in magnetic systems using both XAS and electron energy-loss spectroscopy [36–38], and have been associated with the evolution in the magnitude of the local magnetic moment [35]. Tentatively, we suggest the increase in the branching ratio observed here for $LaVO_3$ reflects the increase in the mean magnitude of the local moment that develops in the low-temperature AFM phase. Future measurements will be made to firmly establish the detailed behaviour of the branching ratio across the transitions of several RVO_3 members.

At the O K-edge, shown in the right panel of figure 5, the relative intensity of feature c (V e_g) is suppressed at 90 K, whereas that of feature a (V $t_{2g\uparrow}$) is somewhat enhanced. Additionally, the energies of features d and e shift upwards by ∼0.3 eV upon cooling down to ∼90 K. According to the x-ray diffraction (XRD) and neutron powder diffraction (NPD) study of $LaVO_3$ by Bordet *et al* [39], the average ⟨V–O⟩ bond length of $LaVO_3$ does not significantly change and the average ⟨La–O⟩ bond length is contracted by only ∼0.01 Å (0.35%) across the transition, although the unit-cell volume of $LaVO_3$ shrinks by ∼1.8 $Å^3$ (almost 1%) upon cooling down to 100 K. We attribute the intensity variation of the unoccupied O 2p–V 3d states and the upward energy shift of O 2p–R 5d hybridization to the structural phase transition from orthorhombic structure ($Pbnm$) to monoclinic structure ($P2_1/a$), which occurs at ∼143 K for $LaVO_3$ [40].

3.3. X-ray emission spectroscopy

The XES process involves the non-resonant excitation of the system by an initial photon and the detection of the emitted photon that accompanies the subsequent decay of a valence electron to fill the core hole. When the incident photon energy is great enough to ionize the core electron, the excited electron does not participate in the emission process, and the occupied PDOS of the valence band (VB) is measured with orbital-, element- and site-specificity. For example, at the O K-edge, non-resonant XES measures the occupied O 2p PDOS of the VB, owing to the transitions from occupied O 2p orbitals to the O 1s core level. As a photon-in and photon-out technique, XES is a bulk-sensitive probe, with a sampling depth of typically ∼100 nm [41].

Figure 6(a) presents normalized above-threshold ($h\nu$ = 550 eV) XES spectra at the O K-edge of $La_{1-x}Lu_xVO_3$, measured at both room temperature and low temperature (∼95 K). These spectra exhibit a strong dependence on x, even at room temperature where all samples are unambiguously in the same phase. A narrow, multiply-peaked structure in $LaVO_3$ develops into a broader spectrum in $LuVO_3$, with a smooth evolution for the intermediate compounds. For comparison, the O 2p PDOS of $LaVO_3$ and $LuVO_3$ from the LSDA + U calculations are shown in figure 6(b), after convolution with a Lorentzian (HWHM = 0.22 eV) and Gaussian (FWHM = 0.37 eV). Although the intensity of the non-bonding peak (k in figure 6(a)) is strongly underestimated by

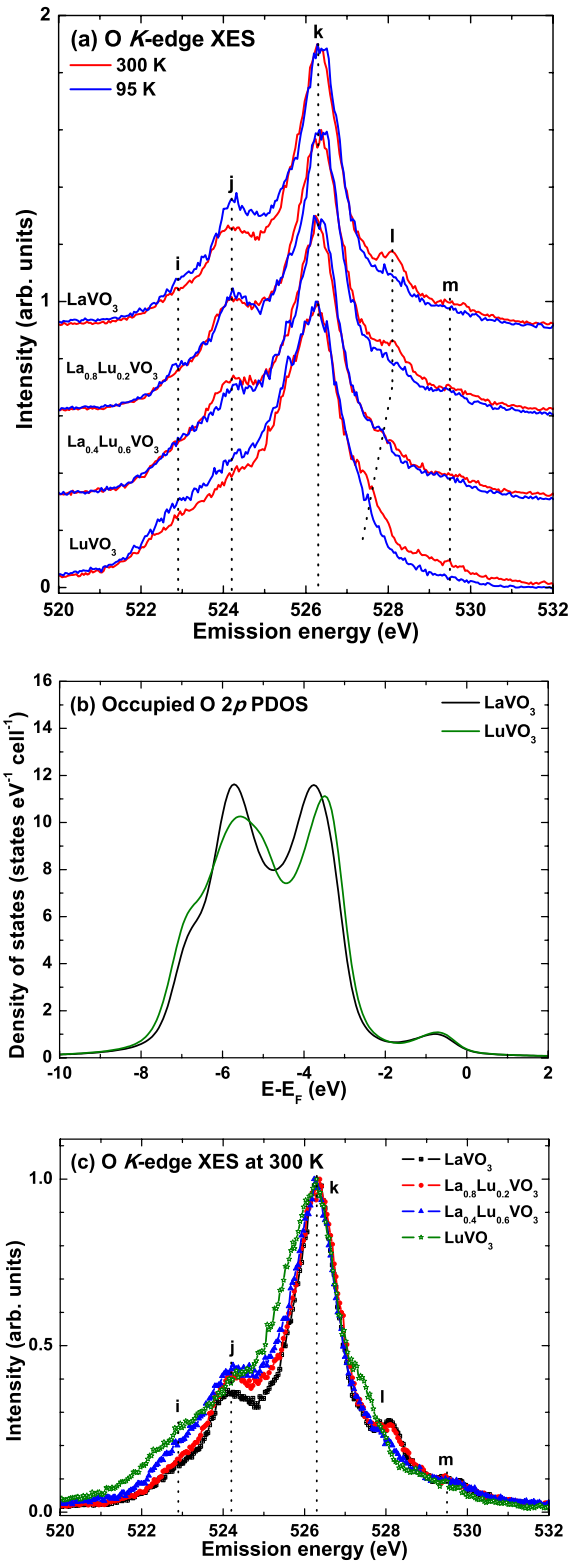

Figure 6. (a) Normalized above-threshold ($h\nu$ = 550 eV) O K-edge XES spectra of $La_{1-x}Lu_xVO_3$ (x = 0, 0.2, 0.6 and 1) recorded at both ∼300 K (red solid lines) and ∼95 K (blue solid lines). The photon energies of the O K-edge XES spectral features i–m are indicated by dotted lines. (b) Theoretical (and broadened) LSDA + U O 2p PDOS of $LaVO_3$ (black solid line) and $LuVO_3$ (olive solid line). (c) A direct comparison between the room temperature XES spectra to show their dependence on the rare-earth ion, R.

the FLAPW calculation (similar to results in other perovskite vanadates [20]), the energies and relative intensities of other PDOS features (i, j and m) in the room temperature spectra are described well by the theory.

The main emission peak k, centred at ∼526.3 eV, arises from non-bonding O 2p states, and features i (∼522.9 eV) and j (∼524.2 eV) originate from hybridized O 2p–V 3d bonding states. In addition, feature m (529.5 eV) can be associated with the weak mixing of the O 2p states with the V 3d states (lower Hubbard band, LHB), which are predicted at $E - E_F = -0.7$ eV from our calculations. These states have been observed directly at ~ -1.5 eV in $LaVO_3$ and YVO_3 photoemission measurements [28, 30] and cluster calculations [31]. We note that this allocation of the O 2p states is in good agreement with previous theoretical studies of $LaVO_3$ and YVO_3 [31, 42]. Finally, approximately 2 eV above the main emission peak, feature l occurs at an energy that does not correspond to any feature in our theoretical PDOS, and is a satellite associated with the double ionization of the O ion (leading to a $2p^{-2}$ final state) during the XES process [43].

Focusing first on the room temperature spectra, which are compared directly in figure 6(c), the O K-edge XES spectra exhibit a strong dependence on the rare-earth ion, R. Overall, the widths of the spectra gradually broaden from $LaVO_3$ to $LuVO_3$, particularly feature j, and the line shape of the main emission peak k becomes more asymmetric. These aspects can be understood from the PDOS, which illustrates the broadening of the bonding O 2p states, and indeed the entire O 2p bandwidth, in $LuVO_3$ compared with $LaVO_3$. In fact, corresponding calculations of YVO_3 in both $LaVO_3$ and $LuVO_3$ crystal structures ($Y_{La}VO_3$ and $Y_{Lu}VO_3$, respectively) display the same trend, indicating this evolution arises from the increased V–O hybridization in $LaVO_3$ due to the crystal structure (rather than the specific choice of rare earth). Finally, feature m remains almost unchanged with R-site cation, suggesting the V 3d LHB is relatively constant across the series, in agreement with photoemission results [44].

Turning to the temperature dependence, for the pure compounds, feature l in particular, and m to a lesser extent, are suppressed at low temperature, whereas features i and j become enhanced. However, the XES spectra of the mixed compounds exhibit much weaker temperature dependence, particularly in the low-energy features i and j. In both pure compounds, the crystal structure evolves from orthorhombic ($Pbnm$) at room temperature to monoclinic ($P2_1/a$) at 95 K, whereas this structural transition is absent in the mixed compounds owing to the suppression of G-type OO. Therefore, the relative enhancement of the V 3d–O 2p bonding features (i and j) in the pure compounds at low temperature indicates a stronger V–O hybridization in the low-temperature monoclinic phase, in agreement with the enhancement of the V $t_{2g\uparrow}$ peak in the XAS spectra.

3.4. Resonant inelastic x-ray scattering

When the incident photon energy is tuned in the vicinity of the absorption threshold, for example at the transition-metal L-edge, the excited electron in the intermediate state strongly affects the emission of a valence electron (governed by dipole selection rules) in the final state and an excitonic state (i.e. a coupled electron–hole pair) is left around the Fermi level. This is referred to as RIXS and the resonant term of the Kramers–Heisenberg equation dominates the differential scattering cross-section [45]. For instance, in a V^{3+} d^2 system, the RIXS excitation process is $2p^63d^2 \rightarrow 2p^53d^3 \rightarrow 2p^63d^{2*}$, where the * in the final state represents an excited configuration of the d^2 ion. Therefore, RIXS explores low-energy excitations, such as local crystal-field excitations (dipole-forbidden dd^* transitions) and charge-transfer excitations. In addition to these loss features, fluorescence (PDOS) features and elastic scattering are also detected in a RIXS spectrum. By examining their dependence on the incident photon energy, the loss features (of constant energy transfer) can be separated from the PDOS features (of constant emission energy).

To begin with, we present a brief overview of the RIXS features, in particular the crystal-field excitations, and their intensity variations with incident photon energy. Figure 7 displays V L_3-edge RIXS spectra of $LaVO_3$ recorded over a broad energy range with moderate resolution ($\Delta E = 0.42$ eV FWHM) at room temperature. The excitation energies were varied across the V L_3-edge absorption peak and selected to be resonant with features in the XAS spectrum. The strong and sharp peak located at high emission energy arises from the elastic scattering of the incident x-rays, which coincides with the incident photon energy in figure 7(a). The broad feature centred at ∼507 eV originates from V 3d–O 2p hybridization. All RIXS spectra presented here have been normalized to the low-energy side of this V 3d–O 2p hybridized feature to facilitate comparison between spectra recorded at different energies, and between different compounds and instruments. The RIXS spectrum excited above the V L_3-edge absorption peak ($h\nu = 520.8$ eV) identifies the emission energy location of pure V 3d states, as well as an overlapping contribution from V 3d–O 2p fluorescence due to L_2-edge emission, which are located at ∼513 eV of emission energy. Dispersive features are also observed in figure 7(a), separated by between ∼−4 and ∼−1 eV from elastic scattering, and represent crystal-field dd^* excitations.

The RIXS spectra are reproduced in figure 7(b) on a loss energy scale. Five major groups of crystal-field excitations, located at ~ -1.0 eV (dd_1^*), ~ -1.8 eV (dd_2^*), ~ -2.4 eV (dd_3^*), ∼−2.8 eV (dd_4^*), and ∼−3.8 eV (dd_5^*) in loss energy, are resolved in figure 7(b). These excitations become clearer after the spectra are deconvoluted using a maximum entropy based deconvolution (MaxEnt) procedure (also shown in figure 7(b)), which has recently been shown to significantly enhance the identification of RIXS features with good signal-to-noise ratio [15]. Although the dd_3^* transition is nearly buried underneath the broad structure of neighbouring transitions, the existence of this feature is suggested by the crystal field multiplet model of RVO_3, for example the recent study of $NdVO_3$ [14], and is directly visible in the spectrum excited at 513.6 eV. Following the analysis of the multiplet model of [14], transitions dd_1^* and dd_3^* can be associated with excitations of the V t_{2g} electrons and transitions dd_2^* and dd_4^* with both t_{2g} and e_g resonances. The higher energy transition (dd_5^*) is connected with excitations into an e_g^2 final configuration.

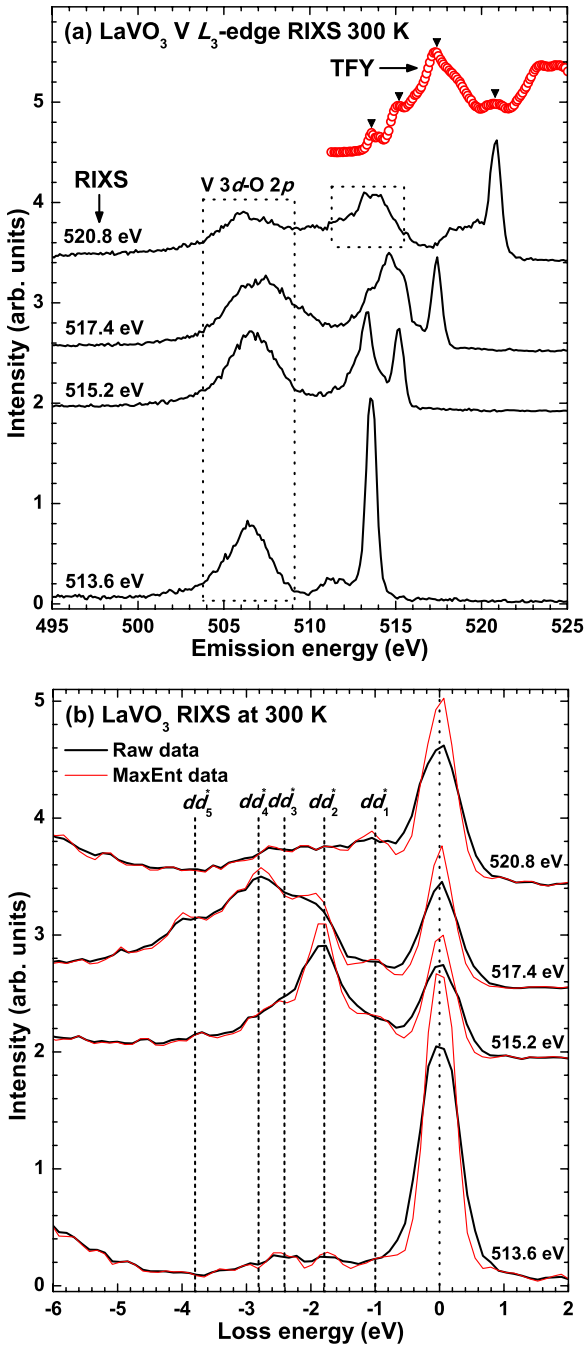

Figure 7. The normalized V L_3-edge RIXS spectra of $LaVO_3$ measured at room temperature (*a*) on an emission energy scale and (*b*) on a loss energy scale. In (*a*), the corresponding XAS (TFY) spectrum (red open circles) is displayed at the top right and the RIXS excitation energies are marked with black triangles on the XAS spectrum. The occupied V 3d states and their hybridization with O 2p states are highlighted with dotted boxes in (*a*). In (*b*), the raw data (black solid lines) are shown together with the results of the MaxEnt procedure (red, light solid lines). The energy locations of the principal dd* transitions are indicated by vertical short dashed lines.

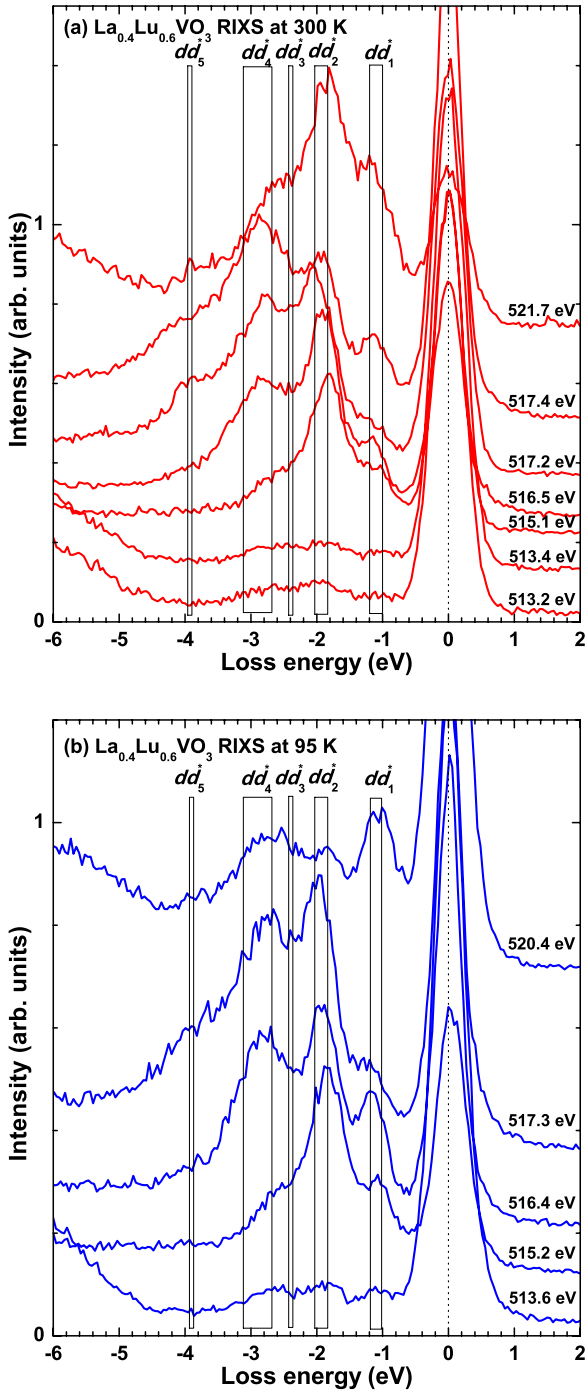

Figure 8. The normalized V L_3-edge RIXS spectra of $La_{0.4}Lu_{0.6}VO_3$ recorded (*a*) at 300 K (red solid lines) and (*b*) at 95 K (blue solid lines) are displayed on a loss energy scale. The incident photon energies are varied across the V L_3-edge absorption spectra. The energy locations and splitting of dd* excitations are indicated by vertical bars in proportion to their approximate width.

The energy location and splitting of the dd* transitions of all compounds are now investigated using high-resolution (ΔE = 0.34 eV FWHM) RIXS measurements. Figure 8 shows representative V L_3-edge RIXS spectra of $La_{0.4}Lu_{0.6}VO_3$ collected at both room temperature and low temperature (~95 K). The same crystal-field excitations that were identified in figure 7 are now much better resolved, and the energy locations of these spectral features present visible energy splitting, which is indicated by the vertical bars in figure 8. The symmetries of the dd* transitions of RVO_3 have been assigned by means of the crystal-field multiplet model (see [14]). The group of transitions dd^*_1 originate from

singlet (i.e. spin-flip) t_{2g} excitations of $^1T_2$ and ^1E symmetries. Transitions dd_2^* come from triplet t_{2g}/e_g excitations of $^3T_2$ symmetry. Experimentally, an energy splitting of ~0.2 eV of the $^3T_2$ level is clearly observed in figure 8, whose origin is the distortion of the VO_6 octahedron (and associated splitting of the d_{xy} and $d_{xz,yz}$ levels). Transition dd_3^* is attributed to the singlet t_{2g} excitation of $^1A_1$ symmetry. Lastly, the broad group of transitions dd_4^* are contributed by t_{2g}/e_g configurations of $^3T_1$, $^1T_2$ and $^1T_1$ symmetries. This assignment is also in agreement with a recent high-resolution RIXS study of YVO_3 [13].

Finally, in order to investigate the dependence of crystal-field excitations with *R*-site cation and temperature, a comparative study of high-resolution RIXS is performed across the series of $La_{1-x}Lu_xVO_3$ compounds and at identical temperatures of 300 and 95 K (low temperature). During the measurements, the incident photon energy and the spectrometer resolution were kept fixed and the experimental geometry remained unchanged. Figure 9 presents normalized V L_3-edge RIXS spectra of $La_{1-x}Lu_xVO_3$ compounds recorded at both room temperature and low temperature with excitation energies of 516.4 eV (both t_{2g} and e_g resonance) and 517.3 eV (e_g resonance), respectively.

The relative intensities of the RIXS transitions of $La_{1-x}Lu_xVO_3$ shown in figure 9 display pronounced temperature dependence: the majority of crystal-field excitations and elastic peaks are enhanced at 95 K compared to those at 300 K, although the evolution of some individual transitions are not clear. This is similar to the change of the optical strength of the dimer excitations in the low-temperature phase of YVO_3 [11]. In both cases, the variation of the strength of either intrasite or intersite dd* transitions reflects the change of the electron transition probability in the spin-ordered and orbital-ordered states of RVO_3, as well as the altered V local environment due to the strong anisotropy in V–O bond lengths with the formation of JT distortion [3, 4, 39, 46].

The energies of dd* transitions is further determined from the RIXS spectra by fitting the spectra to a superposition of Gaussian functions, and the fitting results are given in figure 10. At room temperature, the dd* energy displays an approximately linear dependence with *R*-site ionic size, as demonstrated in figure 10(*a*). With the decrease of the average rare-earth size, the energies of transitions dd_1^*, dd_2^* and dd_4^* are found to slightly increase by up to ~0.1 eV and an energy increase of ~0.2 eV is observed for transition dd_5^*. Since the dd* energy directly reflects the energy splitting of V 3d orbitals, our results suggest that the V 3d orbital splitting of $La_{1-x}Lu_xVO_3$ is gradually enhanced with the decreasing average rare-earth radius. The greater V 3d energy splitting of smaller rare-earth compound here is attributed to the increased tilting magnitude of V–O–V bond angles, which may lead to the enhanced distortion of the VO_6 octahedron. For the pure RVO_3 compounds, the tilting angle φ of VO_6 octahedron progressively increases from 11.60° to 19.09° with the *R*-site cation varied from La to Lu according to XRD and NPD data [10]. As a representative member of *R*-site substituted RVO_3 compounds, the ⟨V–O–V⟩ bond angles of $Y_{1-x}La_xVO_3$ [6] were found to expand linearly with the increase of average

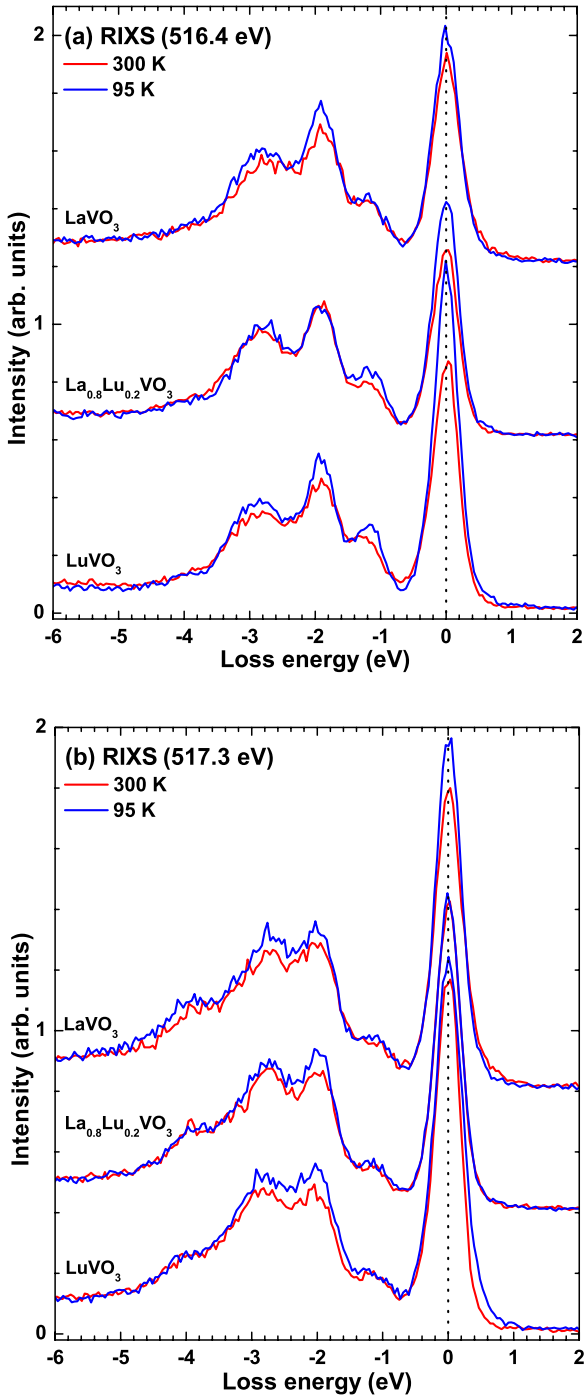

Figure 9. The normalized V L_3-edge RIXS spectra of $La_{1-x}Lu_xVO_3$ ($x = 0$, 0.2 and 1) compounds measured at both 300 K (red solid lines) and 95 K (blue solid lines) with excitation energies of (*a*) 516.4 eV and (*b*) 517.3 eV, respectively, are plotted on loss energy scales.

rare-earth radius. Therefore, it is reasonable to expect an approximate linear increase of tilting angle φ with the decrease of *R*-site ionic size in our mixed $La_{1-x}Lu_xVO_3$ compounds. Nevertheless, the energy locations of dd* excitations are found to change little with temperature for all $La_{1-x}Lu_xVO_3$ compounds. This is in agreement with the very little change in the inter-site dd* band location of YVO_3 upon cooling down across the phase transitions [11].

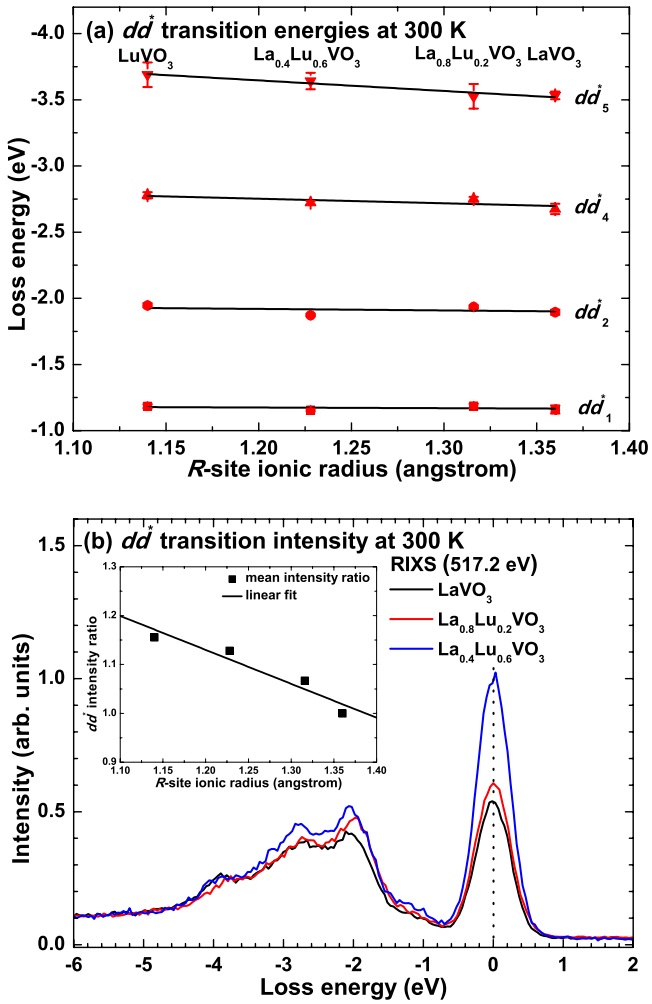

Figure 10. (*a*) The energy positions of dd* transitions at 300 K, determined from the RIXS spectra in figure 9 by fitting to a superposition of Gaussian functions, are displayed as a function of *R*-site ionic radius. The energy locations of transitions dd_1^*, dd_2^*, dd_4^* and dd_5^* are represented by red filled squares, circles, upward triangles and downward triangles, respectively, along with their fitting error bars. The R^{3+}-site size-dependence of the dd* energy is indicated by linear fit. (*b*) The normalized V L_3-edge RIXS spectra of $La_{1-x}Lu_xVO_3$ ($x = 0$, 0.2 and 0.6) compounds recorded at 300 K and with an excitation energy of 517.2 eV are displayed on a loss energy scale. The inset in (*b*) demonstrates the mean intensity ratio ($La_{1-x}Lu_xVO_3$/$LaVO_3$) of the summed spectral strength of dd* transitions as a function of *R*-site ionic radius.

Owing to the arbitrary cleavage planes of the different $La_{1-x}Lu_xVO_3$ compounds during the RIXS measurements, variations in the relative intensities of RIXS features that may be due to the crystal symmetry are difficult to separate from those that arise from the evolution in rare-earth size in these measurements. Nevertheless, three distinctive data sets (BL8 data set 1, BL8 data set 2 and BL7 data set) were measured with different sample orientations to qualitatively investigate the rare-earth size-dependence of the total dd* intensity. During these three measurements, all of which include $LaVO_3$, the incident photon energy was set close to the V L_3-edge main absorption peak. For comparison, all spectra have been normalized to those of $LaVO_3$ and the mean intensity ratio ($La_{1-x}Lu_xVO_3$/$LaVO_3$) of the summed intensity of dd* transitions is displayed as a function of *R*-site ionic radius in the inset of figure 10(*b*). As a representative data set, spectra recorded at room temperature with an excitation energy of 517.2 eV, corresponding to BL8 data set 2, are illustrated in figure 10(*b*). Our results show that the integrated intensity of dd* transitions (and the intensity of elastic peak) are gradually enhanced with the decreasing *R*-site ionic size. This enhancement in the intensity of RIXS features reflects the more localized electronic structure of V 3d electrons in $LuVO_3$. As demonstrated by the LSDA + *U* calculations presented in figure 1, the localization of the V 3d electrons increases from $LaVO_3$ to $LuVO_3$, owing to the progressive increase in the tilt angle of the VO_6 octahedra. In the LSDA + *U* calculations, this is manifested by a narrower V t_{2g} bandwidth in $LuVO_3$, in agreement with this compound being one of the most insulating RVO_3 compounds from resistivity measurements [47]. The enhancement of RIXS intensities with the decrease of *R* radius here is likely related to the increase of V 3d electron localization, which leads to larger electron transition probability.

In the low-temperature OO phase, the RIXS intensities of the mixed $La_{1-x}Lu_xVO_3$ compounds, shown in figure 11, appear suppressed with respect to those of the pure compounds. In figure 11(*a*), RIXS spectra of all $La_{1-x}Lu_xVO_3$ compounds, recorded at 95 K with an incident photon energy of 516.4 eV (both t_{2g} and e_g resonance), are compared to demonstrate this intensity suppression. The relative intensity of the RIXS features, particularly transition dd_2^* (at ~ -1.9 eV), is significantly weaker in the spectra of $La_{0.8}Lu_{0.2}VO_3$ and $La_{0.4}Lu_{0.6}VO_3$ compared to those of $LaVO_3$ and $LuVO_3$.

The observed suppression in the RIXS features of the mixture compounds is likely related to the suppression of *G*-OO due to the SV in $La_{1-x}Lu_xVO_3$. Figure 11(*b*) shows the SO and OO temperatures of $LaVO_3$ [16, 21] and $LuVO_3$ [2] obtained from previous studies, as well as those of $La_{0.8}Lu_{0.2}VO_3$ and $La_{0.4}Lu_{0.6}VO_3$ determined from our magnetization and heat-capacity measurements. Typically, the disorder associated with the SV is expected to suppress long-range (spin or orbital) order, as occurs for the rare-earth manganites [48]. However, as illustrated by [5, 6], although *C*-SO and *G*-OO are indeed suppressed, unlike the manganites a different ordering pattern (*G*-SO/*C*-OO) is instead stabilized in RVO_3. Those authors attribute this effect to the long-range disruption of the 1D chains in the *C*-SO/*G*-OO pattern for large SV, at which point the alternative ordering becomes energetically favourable. At 95 K, the temperature at which the RIXS spectra were collected, the two pure compounds are both in the *G*-OO phase, whereas $La_{0.4}Lu_{0.6}VO_3$ is in the *C*-OO phase. For $La_{0.8}Lu_{0.2}VO_3$, our measurements confirm the suppression of *G*-OO, although whether *C*-OO is fully formed is unclear. As discussed above, consistent, though weak, spectral changes with *R* are found in the V *L*-edge XAS and RIXS spectra recorded at room temperature, for which the *R* size effect is dominant. However, the RIXS spectra collected at 95 K, when the V t_{2g} orbital-ordered states were formed, do not continuously increase their intensity with decreasing *R* radius and display suppressed intensity for the mixed compounds with respect to the pure compounds. This intensity suppression at

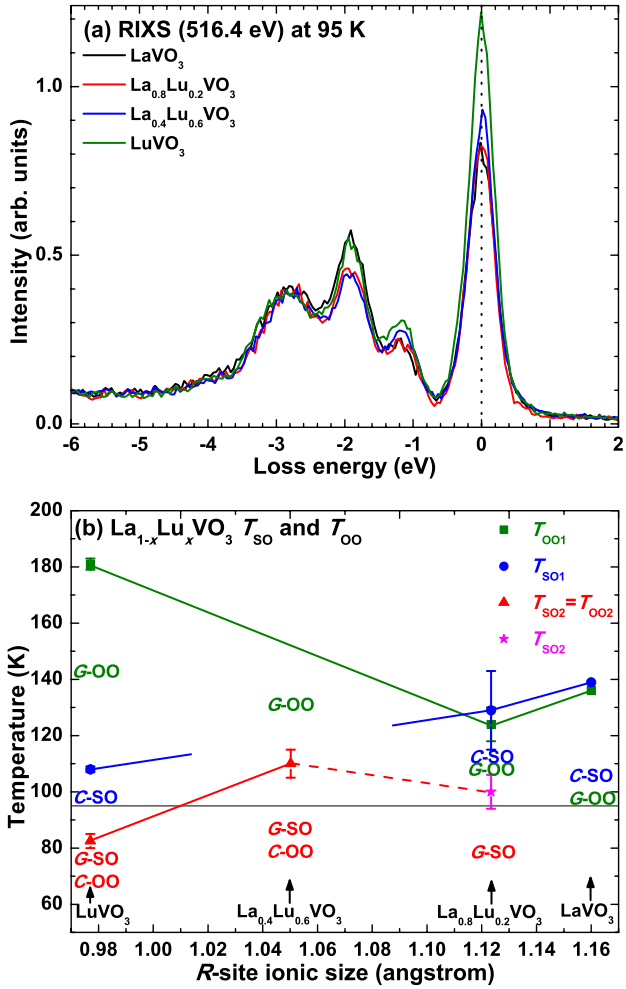

Figure 11. (*a*) The normalized V L_3-edge RIXS spectra of all $La_{1-x}Lu_xVO_3$ compounds measured at 95 K and with an excitation energy of 516.4 eV are compared on a loss energy scale. (*b*) SO and OO temperatures of $La_{1-x}Lu_xVO_3$, T_{OO1} (olive filled squares), T_{SO1} (blue filled circles), $T_{SO2} = T_{OO2}$ (red filled triangles), and T_{SO2} only (magenta filled star), determined from the magnetization and heat-capacity data of this study and previous studies (see [2, 21]), are displayed as a function of R-site ionic size, along with their error bars.

95 K is likely related to different OO phases in $La_{1-x}Lu_xVO_3$ owing to the R-site SV.

4. Conclusions

The effects of rare-earth size on the electronic structures of $La_{1-x}Lu_xVO_3$ single crystals have been investigated using XAS and XES at the O K-edge and RIXS at the V L_3-edge. The variations in the O 2p PDOS with R-site cation observed in the O K-edge spectra, such as the upward energy shift of the unoccupied O 2p–R 5d hybridization states and the broadening of the occupied O 2p states from La to Lu, are explained well by LSDA+U calculations of the pure compounds. This evolution with R, together with the temperature dependence of the O K-edge spectra, is attributed to modifications in the crystal structure of $La_{1-x}Lu_xVO_3$. With the decrease in R radius, the crystal-field dd* transitions, detected by RIXS, increase in both energy and relative intensity, which we attribute to the increase in the VO_6 tilting magnitude. For all compounds, the increase of the RIXS spectral intensity upon cooling down to the low-temperature OO phase agrees with the formation of the JT distortion. However, the suppression in the intensity of RIXS features in the mixture compounds with respect to the pure compounds at 95 K is likely connected with the suppression of G-type OO and the incomplete formation of C-type OO in $La_{1-x}Lu_xVO_3$.

Acknowledgments

The Boston University program is supported by the Department of Energy under Grant No. DE-FG02-98ER45680. The Advanced Light Source is supported by the Director, Office of Science, Office of Basic Energy Sciences, of the US Department of Energy under Contract No. DE-AC02-05CH11231. GB gratefully acknowledges financial support from EPSRC Grant EP/I007210/1. This project is also supported in part by the Boston University/University of Warwick collaboration fund.

References

[1] Miyasaka S, Fujioka J, Iwama M, Okimoto Y and Tokura Y 2006 Raman study of spin and orbital order and excitations in perovskite-type RVO_3 (R = La, Nd, and Y) *Phys. Rev.* B **73** 224436

[2] Miyasaka S, Okimoto Y, Iwama M and Tokura Y 2003 Spin-orbital phase diagram of perovskite-type RVO_3 (R = rare-earth ion or Y) *Phys. Rev.* B **68** 100406

[3] Blake G R, Palstra T T M, Ren Y, Nugroho A A and Menovsky A A 2001 Transition between orbital orderings in YVO_3 *Phys. Rev. Lett.* **87** 245501

[4] Sage M H, Blake G R, Marquina C and Palstra T T M 2007 Competing orbital ordering in RVO_3 compounds: high-resolution x-ray diffraction and thermal expansion *Phys. Rev.* B **76** 195102

[5] Fukuta R *et al* 2011 Effects of cation-size variance on spin and orbital orders in $Eu_{1-x}(La_{0.254}Y_{0.746})_xVO_3$ *Phys. Rev.* B **84** 140409

[6] Yan J-Q *et al* 2007 Orbital fluctuations and orbital flipping in RVO_3 perovskites *Phys. Rev. Lett.* **99** 197201

[7] Noguchi M, Nakazawa A, Oka S, Arima T, Wakabayashi Y, Nakao H and Murakami Y 2000 Synchrotron x-ray-diffraction study of orbital ordering in YVO_3 *Phys. Rev.* B **62** R9271–4

[8] Bizen D, Nakatsuka K, Murata T, Nakao H, Murakami Y, Miyasaka S and Tokura Y 2008 Orbital ordering in RVO_3 (R = Y, Tb) controlled by hydrostatic pressure *Phys. Rev.* B **78** 224104

[9] Fujioka J, Miyasaka S and Tokura Y 2005 Orbital disordering and the metal–insulator transition with hole doping in perovskite-type vanadium oxides *Phys. Rev.* B **72** 024460

[10] Martínez-Lope M J, Alonso J A, Retuerto M and Fernández-Díaz M T 2008 Evolution of the crystal structure of RVO_3 (R = La, Ce, Pr, Nd, Tb, Ho, Er, Tm, Yb, Lu, Y) perovskites from neutron powder diffraction data *Inorg. Chem.* **47** 2634–40

[11] Tsvetkov A A, Mena F P, van Loosdrecht P H M, van der Marel D, Ren Y, Nugroho A A, Menovsky A A, Elfimov I S and Sawatzky G A 2004 Structural, electronic, and magneto-optical properties of YVO_3 *Phys. Rev.* B **69** 075110

[12] Benckiser E, Rückamp R, Möller T, Taetz T, Möller A, Nugroho A A, Palstra T T M, Uhrig G S and Grüninger M

2008 Collective orbital excitations in orbitally ordered YVO_3 and $HoVO_3$ *New J. Phys.* **10** 053027
[13] Benckiser E *et al* 2013 Orbital superexchange and crystal field simultaneously at play in YVO_3: resonant inelastic x-ray scattering at the V *L* edge and the O *K* edge *Phys. Rev.* B **88** 205115
[14] Laverock J *et al* 2014 Low-energy V t_{2g} orbital excitations in $NdVO_3$ *J. Phys.: Condens. Matter* **26** 455603
[15] Laverock J, Preston A R H, Newby D Jr, Smith K E and Dugdale S B 2011 Maximum entropy deconvolution of resonant inelastic x-ray scattering spectra *Phys. Rev.* B **84** 235111
[16] Tung L D, Lees M R, Balakrishnan G and Paul D McK 2007 Magnetization reversal in orthovanadate RVO_3 compounds (R = La, Nd, Sm, Gd, Er, and Y): inhomogeneities caused by defects in the orbital sector of quasi-one-dimensional orbital systems *Phys. Rev.* B **75** 104404
[17] Chen X, Glans P-A, Qiu X, Dayal S, Jennings W D, Smith K E, Burda C and Guo J 2008 X-ray spectroscopic study of the electronic structure of visible-light responsive N-, C- and S-doped TiO_2 *J. Electron Spectrosc. Relat. Phenom.* **162** 67–73
[18] Dewhurst J K, Sharma S, Nordström L, Cricchio F, Bultmark F and Gross E K U 2012 *The Elk Code Manual* http://elk.sourceforge.net
[19] Shim J H, Kang J S and Min B I 2004 Electronic structures of RTe_2 (R = La, Ce): a clue to the pressure-induced superconductivity in $CeTe_{1.82}$ *Phys. Rev. Lett.* **93** 156406
[20] Laverock J, Chen B, Preston A R H, Smith K E, Wilson N R, Balakrishnan G, Glans P-A and Guo J-H 2013 Electronic structure of the Kagome staircase compounds $Ni_3V_2O_8$ and $Co_3V_2O_8$ *Phys. Rev.* B **87** 125133
[21] Tung L D, Ivanov A, Schefer J, Lees M R, Balakrishnan G and Paul D M 2008 Spin, orbital ordering, and magnetic dynamics of $LaVO_3$: magnetization, heat capacity, and neutron scattering studies *Phys. Rev.* B **78** 054416
[22] de Groot F M F, Grioni M, Fuggle J C, Ghijsen J, Sawatzky G A and Petersen H 1989 Oxygen 1s x-ray-absorption edges of transition-metal oxides *Phys. Rev.* B **40** 5715–23
[23] Mauchamp V, Jaouen M and Schattschneider P 2009 Core-hole effect in the one-particle approximation revisited from density functional theory *Phys. Rev.* B **79** 235106
[24] Chen B *et al* 2013 The band structure of WO_3 and non-rigid-band behaviour in $Na_{0.67}WO_3$ derived from soft x-ray spectroscopy and density functional theory *J. Phys.: Condens. Matter* **25** 165501
[25] de Groot F 2005 Multiplet effects in x-ray spectroscopy *Coord. Chem. Rev.* **249** 31–63
[26] van der Laan G and Kirkman I W 1992 The 2p absorption spectra of 3d transition metal compounds in tetrahedral and octahedral symmetry *J. Phys.: Condens. Matter* **4** 4189–204
[27] Achkar A J, Regier T Z, Wadati H, Kim Y J, Zhang H and Hawthorn D G 2011 Bulk sensitive x-ray absorption spectroscopy free of self-absorption effects *Phys. Rev.* B **83** 081106
[28] Pen H F, Abbate M, Fuijmori A, Tokura Y, Eisaki H, Uchida S and Sawatzky G A 1999 Electronic structure of $Y_{1-x}Ca_xVO_3$ studied by high-energy spectroscopies *Phys. Rev.* B **59** 7422–32
[29] Purans J, Kuzmin A, Parent P and Laffone C 1998 Study of the electronic structure of rhenium and tungsten oxides on the O *K*-edge *Ionics* **4** 101–5
[30] Maiti K and Sarma D D 2000 Spectroscopic investigations of the electronic structure and metal–insulator transitions in a Mott–Hubbard system $La_{1-x}Ca_xVO_3$ *Phys. Rev.* B **61** 2525
[31] Mossanek R J O, Abbate M, Fonseca P T, Fujimori A, Eisaki H, Uchida S and Tokura Y 2009 Optical conductivity and x-ray absorption spectra of the Mott–Hubbard compounds RVO_3 (R = Sr, Ca, La, and Y) *Phys. Rev.* B **80** 195107
[32] Piper L F J, DeMasi A, Cho S W, Preston A R H, Laverock J, Smith K E, West K G, Lu J W and Wolf S A 2010 Soft x-ray spectroscopic study of the ferromagnetic insulator $V_{0.82}Cr_{0.18}O_2$ *Phys. Rev.* B **82** 235103
[33] Schmitt T, Duda L-C, Matsubara M, Augustsson A, Trif F, Guo J-H, Gridneva L, Uozumi T, Kotani A and Nordgren J 2004 Resonant soft x-ray emission spectroscopy of doped and undoped vanadium oxides *J. Alloys Compounds* **362** 143–50
[34] Wadati H, Hawthorn D G, Geck J, Regier T Z, Blyth R I R, Higuchi T, Hotta Y, Hwang H Y and Sawatzky G A 2009 Interface reconstruction in V-oxide heterostructures determined by x-ray absorption spectroscopy *Appl. Phys. Lett.* **95** 023115
[35] Thole B T and van der Laan G 1988 Branching ratio in x-ray absorption spectroscopy *Phys. Rev.* B **38** 3158–71
[36] Liu M T *et al* 2008 Correlation between magnetic properties and the electronic structures of soft magnetic ternary $Fe_{78-x}Y_xB_{22}$ ($x = 4 - 9$) bulk metallic glasses *J. Phys.: Condens. Matter* **20** 465105
[37] Morrison T I, Brodsky M B, Zaluzec N J and Sill L R 1985 Iron *d*-band occupancy in amorphous Fe_xGe_{1-x} *Phys. Rev.* B **32** 3107–11
[38] Wang H J, Gu X J, Poon S J and Shiflet G J 2008 Electronic structure of Fe-based amorphous alloys studied using electron-energy-loss spectroscopy *Phys. Rev.* B **77** 014204
[39] Bordet P, Chaillout C, Marezio M, Huang Q, Santoro A, Cheong S-W, Takagi H, Oglesby C S and Batlogg B 1993 Structural aspects of the crystallographic–magnetic transition in $LaVO_3$ around 140 K *J. Solid State Chem.* **106** 253–70
[40] Ren Y, Nugroho A A, Menovsky A A, Strempfer J, Rütt U, Iga F, Takabatake T and Kimball C W 2003 Orbital-ordering-induced phase transition in $LaVO_3$ and $CeVO_3$ *Phys. Rev.* B **67** 014107
[41] Smith K E, McGuinnes C, Downes J E, Ryan P J, Fu D, Hulbert S L, Honig J M and Egdell R G 2003 Soft x-ray emission and resonant inelastic x-ray scattering studies of transition metal oxides *Mater. Res. Soc. Symp. Proc.* **755** DD1
[42] Mizokawa T and Fujimori A 1996 Electronic structure and orbital ordering in perovskite-type 3d transition-metal oxides studied by Hartree–Fock band-structure calculations *Phys. Rev.* B **54** 5368
[43] Anisimov V I, Kuiper P and Nordgren J 1994 First-principles calculation of NiO valence spectra in the impurity-Anderson-model approximation *Phys. Rev.* B **50** 8257–65
[44] Mossanek R J O, Abbate M, Yoshida T, Fujimori A, Yoshida Y, Shirakawa N, Eisaki H, Kohno S and Vicentin F C 2008 Evolution of the spectral weight in the Mott–Hubbard series $SrVO_3$–$CaVO_3$–$LaVO_3$–YVO_3 *Phys. Rev.* B **78** 075103
[45] Kotani A and Shin S 2001 Resonant inelastic x-ray scattering spectra for electrons in solids *Rev. Mod. Phys.* **73** 203–46
[46] Muñoz A, Alonso J A, Casais M T, Martínez-Lope M J, Martínez J L and Fernández-Díaz M T 2004 Thermal evolution of the crystallographic and magnetic structure in $LuVO_3$: a neutron diffraction study *Chem. Mater.* **16** 1544–50
[47] Sakai T, Adachi G, Shiokawa J and Shin-ike T 1976 Electrical conductivity of $LnVO_3$ compounds *Mater. Res. Bull.* **11** 1295–9
[48] Tomioka Y and Tokura Y 2004 Global phase diagram of perovskite manganites in the plane of quenched disorder versus one-electron bandwidth *Phys. Rev.* B **70** 014432